# Injectable Temperature Sensors Based on Passive Rectification of Volume-Conducted Currents

Laura Becerra-Fajardo*, Aracelys García-Moreno*, Nerea Alvarez de Eulate Llano*, and Antoni Ivorra*†.
Email: laura.becerra@upf.edu aracelys.garcia@upf.edu antoni.ivorra@upf.edu
*Department of Information and Communication Technologies, Universitat Pompeu Fabra. Barcelona, Spain.
†Serra Húnter Programme, Universitat Pompeu Fabra, Barcelona, Spain.

***Abstract*— *In situ* monitoring of biomedical parameters with implantable sensors can provide information to trigger interventional or therapeutic actions. However, these sensors require bulky components for power or for interrogation that hinder miniaturization. We have proposed a wireless sensing method based in passive rectification of high frequency current bursts that flow through the tissues by volume conduction. Here we report the evaluation of a 0.98 mm-thick, passive, and flexible temperature sensor based on this method. The injectable microsensor obtained an accuracy of ±2.1%. This opens the possibility of continuous and *in situ* temperature sensing with minimal invasiveness.**

***Keywords—temperature sensor, injectable, wireless, volume conduction, biomedical sensor***

## I. INTRODUCTION

Continuous sensing of biomedical parameters directly measured on the target location can provide reliable information to trigger alarms and perform interventional or therapeutic actions in case of adverse events [1]. For example, early detection of wound infections using quantitative data based on implantable temperature sensors could improve and accelerate the diagnosis and treatment, improving the quality of life of patients, and decreasing the costs related to inaccurate and untimely wound infection diagnosis [2]. Implantable temperature sensors are also proposed for orthopedic implants: temperature may estimate the implant wear rate [3] and detect tissue damage and implant loosening [4]. Furthermore, during some treatments as focused ultrasound ablation, it is also crucial to monitor temperature in the target tissues. To do so, clinicians rely on noninvasive techniques, as magnetic resonance imaging, whose measurements are indirect, require complex and voluminous equipment, and are accompanied by incompatibility issues. They also rely on conventional invasive devices, which are based on probes, being very intrusive and bulky [5]. All this makes convenient the development of minimally invasive temperature sensors that could be used in such scenarios.

Current implantable sensing systems require bulky components within the implant that hinder their miniaturization. On the one hand, active implantable sensors require electrical energy that is usually supplied by batteries or by wireless power transfer (WPT) methods that need coils or other bulky energy transducers, limiting their size and spatial applicability [6][7]. For example, in [8] an implantable temperature sensor powered by NFC is proposed, containing a square-shaped coil of 25 mm × 25 mm. On the other hand, sensors with passive electronics also typically require large components for interrogation. These passive sensors are usually based on the combination of inductors and capacitors that resonate when an alternating magnetic field is applied. The resonant frequency obtained depends on the physical parameter being measured (e.g., the capacitor is used as a transducer). These passive devices require bulky inductors with a large diameter, such as that required by the implant of the CardioMEMS HF System, which contains a coil of about 3 mm × 8 mm [9].

In [10] we described the development and characterization of a system for measuring the conductivity of tissues surrounding a 0.95 mm-thick, passive, flexible and injectable implant. Here we report the development and *in vitro* evaluation of a novel temperature sensing system based on the same passive sensing method to obtain ultrathin and flexible sensors that could be used for *in situ* temperature monitoring.

## II. METHODS

### A. About the passive temperature sensing method

#### 1) Overview

The proposed temperature measurement system consists of a passive injectable sensor and a portable external unit (Fig. 1). The implantable sensor is shaped as a thin elongated body with two electrodes at opposite ends. It consists of an element with asymmetric conductance (a diode, $D_{im}$), connected in series to a capacitor ($C_{im}$), and in parallel to a resistor whose resistance strongly depends on temperature (i.e., thermistor) that discharges the capacitor in-between bursts. In the particular case of the sensor proposed here, the thermistor is a negative temperature coefficient (NTC) thermistor ($NTC_{im}$ in Fig. 1).

The portable external unit interrogates the implants by delivering innocuous high frequency (HF) alternating currents in the form of bursts through two external electrodes. Via volume conduction, the implant picks up a portion of these HF currents, and are rectified through the diode ($D_{im}$), charging the capacitor ($C_{im}$). Immediately after the burst finishes (hereinafter 'burst cessation'), the capacitor discharges through the implant thermistor ($NTC_{im}$) and through the tissues across the implant electrodes, creating a decaying voltage across them. This decaying voltage, also because of volume conduction, can be sensed across the external electrodes of the external unit.

The temporal characteristics of the decaying voltage depend on 1) the capacitance of the capacitor ($C_{im}$), 2) the resistance of the thermistor ($NTC_{im}$), 3) the impedance of the implant electrodes, and 4) the impedance of the tissues across the implant electrodes.

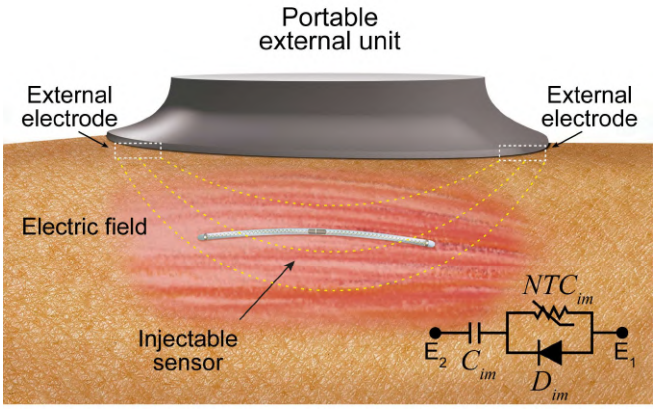


Fig. 1. Schematic representation of a scenario in which temperature is measured using the proposed method. The implant is placed in the target tissues, and two external electrodes deliver high frequency bursts generated by a portable external unit. The external unit produces measurements by measuring and processing the voltage that the implant generates after the burst finishes.

If tissue impedance is approximated to a resistance ($R_{tissue}$), and the impedance of the implant electrodes is neglected, the voltage across the implant electrodes after burst cessation can be expressed as

$$v_{implant}(t) = Ae^{-t/\tau} \quad (1)$$

where A is the initial voltage across the implant electrodes after bursts cessation because of the charge accumulated in $C_{im}$, and the time constant $\tau$ is

$$\tau = C_{im}(NTC_{im} + R_{tissue}) \quad (2)$$

The response of $NTC_{im}$ can be characterized with the beta ($\beta$) parameter and the Steinhart-Hart equation:

$$NTC_{im} = R_0 e^{\beta\left(\frac{1}{T}-\frac{1}{T_0}\right)} \quad (3)$$

where $R_0$ is the resistance of the thermistor at $T_0$ temperature (298.15 K).

Of note, $C_{im}$ not only acts as a charge accumulator for obtaining decaying voltages immediately after burst cessation that are proportional to a measurement, but behaves also as a dc-blocking capacitor to prevent electrochemical reactions that would damage both the electrodes and the tissues.

*2) Measurement of sensed parameter*

The external unit must include a switching mechanism to avoid short-circuiting the decaying voltage signal volume-conducted from the implant in-between bursts. In [10] two antiparallel switching diodes connected in series to the external electrodes are proposed. This mechanism allows the flow of the HF current bursts delivered by the external generator, but blocks the small decaying voltages coming from the implant in-between bursts.

To acquire the decaying signals that are proportional to the voltage across the implant electrodes, the external unit includes a RC low-pass filter (LPF) connected to the external electrodes. This LPF attenuates the voltage seen across the external electrodes (cutoff frequency $F_c$ < 1 MHz) to facilitate digitalization. The voltage across the capacitor of the LPF ($v_L(t)$) will be proportional to the voltage across the implant electrodes, which depends on the temperature measurement given by the implant's thermistor (i.e., $NTC_{im}$). Fig. 2A shows an example of the voltage obtained across the LPF just before burst cessation (time < 100 µs) and after it. Immediately after burst cessation, a very small amplitude decaying waveform is seen (magnification seen in Fig. 2B). This voltage is proportional to the decaying voltage seen at the implant electrodes, and has an amplitude much lower than that measured during the bursts. However, it can be acquired by a data acquisition board (DAQ) for digital processing.

To extract the parameter of interest from such feeble signal, we average multiple acquisitions corresponding to multiple bursts and fit the average recorded signal to a model corresponding to the expected pattern for the implant voltage (1). Fitting can be performed using known curve fitting procedures such as those based on the least squares method.

*3) Compliance with safety standards*

According to international safety standards, there are two adverse health effects of human exposure to electromagnetic currents: unwanted electrostimulation and tissue heating [11]. The threshold for electrostimulation is defined with the dosimetric reference limit (DRL) for the *in situ* electric field, for frequencies between 0 and 5 MHz. In the case of the 3 MHz current burst delivered by the external unit proposed here, the maximum allowed induced *in situ* electric field in brain, heart, limb and other tissues is 883 $V_{rms}$/m, 16940 $V_{rms}$/m, 1880 $V_{rms}$/m and 627 $V_{rms}$/m respectively [11].

In the case of tissue heating, the limits are defined with the Specific Absorption Rate (SAR) which corresponds to

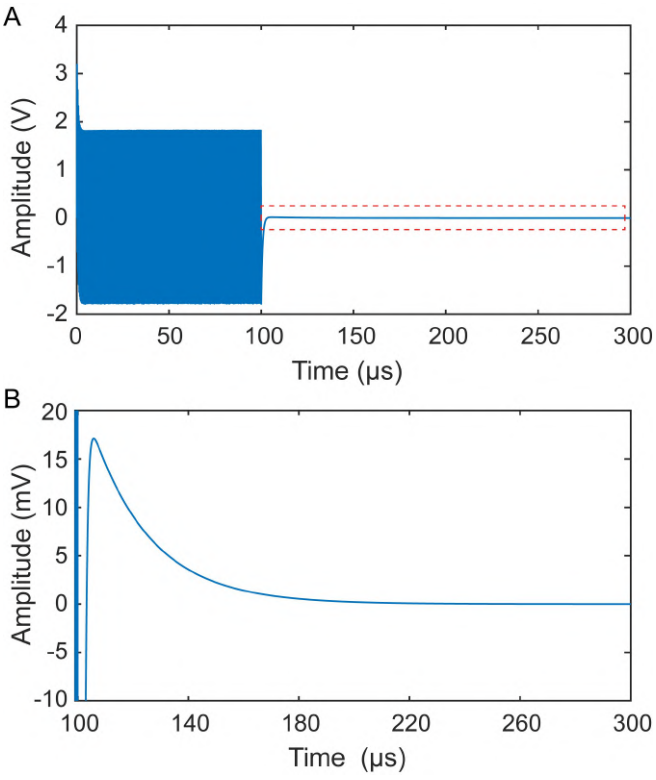


Fig. 2. Voltage obtained across the capacitor of the LPF of the external unit (see Fig. 3). A) HF burst seen in the LPF. When the burst ends, the capacitor of the implant discharges through the NTC thermistor. B) Magnification of the discharge seen from the external unit (red dotted time in A).

the power absorbed per mass of tissue. As mentioned above, the sensing approach proposed here is based on the decaying signal of the voltage across the implant electrodes after bursts cessation. This implies that 1) it is required the use of HF current bursts to obtain these decaying signals, and 2) each measurement reading is associated to the end of one burst. Because of this, the SAR can be minimized by applying short bursts (burst duration $B$ < 200 µs) with a frequency $F$ low enough for the external system to acquire the decaying signal. Then, SAR can be calculated as

$$\mathrm{SAR} = \frac{\sigma\left(\mathrm{E_{peak}}\right)^2}{2\rho} FB \qquad (4)$$

where $E_{peak}$ is the peak electric field applied in the tissues (V/m), $\sigma$ is the electrical conductivity of the tissue (S/m) and $\rho$ is the mass density of the tissue (kg/m$^3$). For this study, the properties of muscle tissue at 3 MHz are used ($\sigma$: 0.57 S/m [12] and $\rho$: 1060 kg/m$^3$ [13]). The SAR limit established for head and torso, and limbs are 2 W/kg, and 4 W/kg respectively.

### B. Simulations

As described and demonstrated in [14], volume conduction can be modeled using a two-port network. In the application considered here, the model is used to simulate the behavior of the circuit for different temperatures, and it is based on the two-port network model thoroughly described in [10]. For easier follow-up of the following sections, it is worth recalling that the $R_{XY}$ two-port network parameters are: $R_{11}$, which corresponds to the resistance between the external electrodes, $R_{12}$, which corresponds to the resistance between the external electrodes and the implant electrodes, and $R_{22}$, which corresponds to the resistance across the implant electrodes ($R_{tissue}$).

The parameters for the network were obtained using a finite element method (FEM) simulation (COMSOL Multiphysics 5.3) using the "Electric Currents" application mode. The geometry of the medium is based on the *in vitro* setup described below. It consists of a cylinder (diameter: 65 mm; length: 110 mm) with electrical properties similar to those of muscle tissue at 3 MHz ($\sigma$: 0.57 S/m, $\varepsilon$: 522 [12]). Two metallic rings acting as external electrodes and separated 100 mm are placed at the ends of the cylinder (width: 10 mm). The implant is centered on the medium, and its geometry is based on the injectable prototype described below. In the simulation, the implant consists of two metallic cylinders (diameter: 0.95 mm, length: 2.5 mm) separated by a silicone cylinder. The distance between centers of electrodes is 26.5 mm.

A parametric SPICE simulation (LTspice XVII by Analog Devices, Inc.) was done using the $R_{XY}$ two-port network parameters obtained from the FEM simulation (Fig. 3). The SPICE simulation included the external unit (i.e., the bursts generator, the switching diodes, and the LPF for reading the decaying voltage across the external electrodes), and the electronic circuitry of the injectable device. The value of the NTC thermistor (3) was parametrized according to an input temperature ranging from 35 °C to 40 °C.

### C. In vitro validation

The injectable prototype was developed using commercially available components soldered on a flexible PCB. The circuit consists of a 10 nF capacitor ($C_{im}$, TMK063BJ103KP-F by Taiyo Yuden), connected in series to the parallel combination of a Schottky diode ($D_{im}$, RB521ZS-30 by ROHM Semiconductor) and a NTC thermistor ($NTC_{im}$, ERT-JZET202H by Panasonic). The thermistor has a nominal resistance at 25 ºC of 2 kΩ ($R_0$) with a tolerance of ±3%, and a beta value ($\beta$) of 4500 K ± 2%. Two Pt-Ir spring wires connect the ends of the circuit to two distal electrodes ($E_1$ and $E_2$ in Fig. 5), which have a length of 2.5 mm, and a diameter of 0.95 mm. The distance between centers of electrodes is 26.5 mm. The entire assembly, except for the electrodes, is housed in a silicone tube, which was finally filled with a low viscosity medical grade silicone elastomer (MED-6015 by NuSil Technology). The total implant length is 30 mm, with an overall diameter of 0.98 mm (Fig. 4).

To test the injectable sensor in a scenario which resembles more closely the body temperature, an *in vitro* experimental setup was implemented (Fig. 5). It consists of an agar cylinder (diameter: 65 mm; length: 110 mm) made from a NaCl solution with a conductivity similar to that of muscle tissue at 3 MHz ($\sigma$: 0.57 S/m [12]). The dimensions of the cylinder are similar to those of a partial section of the forearm of an adult. The cylinder was cut through its sagittal plane to place the implant in its center. The reference temperature measurement consisted of a thermistor (ERT-J1VT202H by Panasonic), soldered to two Kynar wires (100-30BK by PRO POWER), and connected to an ohmmeter (38XR-A by Amprobe). This thermistor was placed very closely to the thermistor integrated in the implant to measure a temperature similar to that measured by the implant's temperature transducer.

After properly locating the implant and the reference thermistor on the center of the cylinder, the devices were covered with the second half of the agar cylinder (implant depth: 3.25 cm). The agar cylinder was then placed in an oven and slowly heated until the reference thermistor measured approximately 42 ºC. The cylinder was then removed from the oven and placed on a test bench for electrical measurements and slow cooling. Measurements

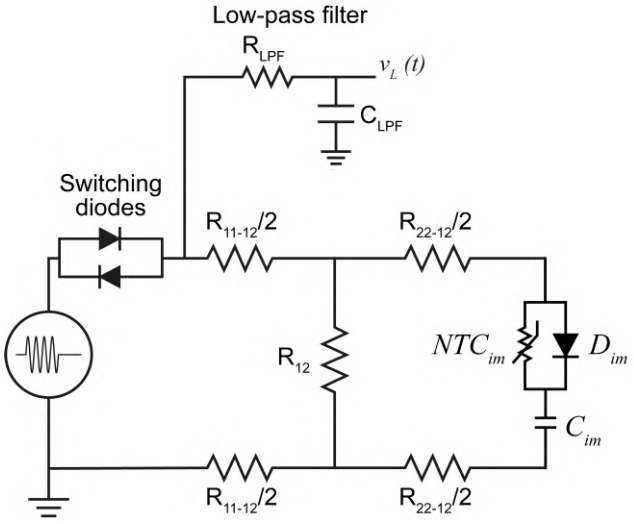


Fig. 3. Two-port network model of the passive rectification of volume-conducted currents for temperature measurement. The network models the coupling between the two external electrodes of the external unit and the two electrodes of the implantable sensor.

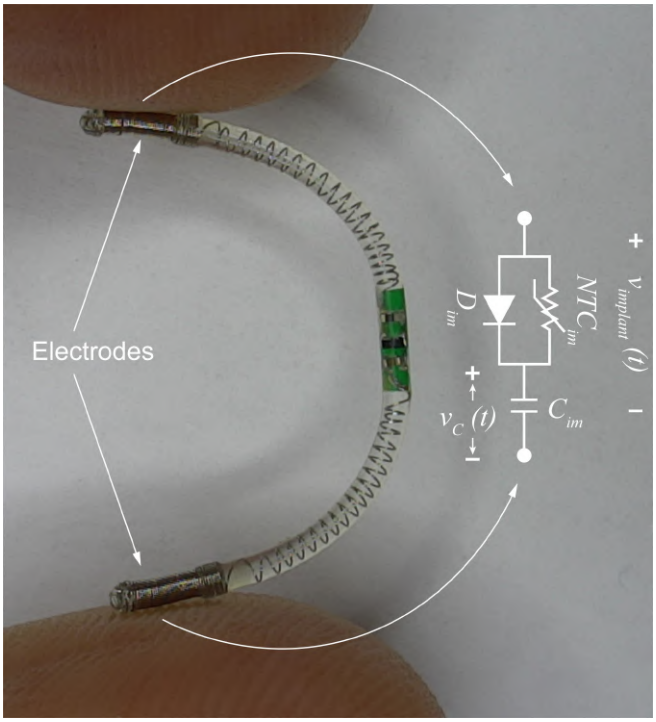


Fig. 4. Injectable temperature sensor developed for the *in vitro* demonstration. It has a diameter of 0.98 mm and a length of 30 mm.

were performed in the range from 40 °C to 33 °C, similar to the range proposed for implantable temperature sensors [15].

Two aluminum band electrodes were strapped around the cylinder, at a distance of 10 cm. The electrodes were connected to an external unit that consisted of 1) a bursts generator composed of a signal generator (BK4064 by BK Precision) followed by a high voltage amplifier, 2) two antiparallel diodes (1N4148 by Vishay Intertechnology, Inc.) acting as switching diodes, 3) a passive RC LPF ($R_{LPF}$: 1.5 kΩ; $C_{LPF}$: 470 pF; $F_c$: 225 kHz), and 4) a DAQ board (NI-USB6216 by National Instruments Corp.) connected to a PC laptop running Matlab (Matlab R2019b).

The DAQ was configured to sample at a frequency of 400 ksps for 100 ms. During this time, 100 burst cessations

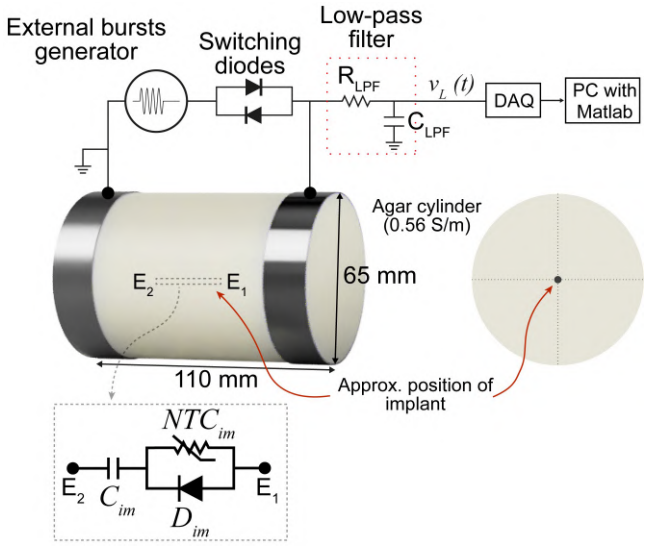


Fig. 5. *In vitro* setup used to test the injectable temperature sensor. The implant is located approximately at the center of an agar cylinder.

were recorded and processed offline. They were synchronized and averaged to obtain a single decaying waveform that represents the voltage seen at the external electrodes for a specific temperature. Finally, an exponential fit based on the nonlinear least squares method was made to obtain the time constant and resistance equivalent to that of the sum of the $NTC_{im}$ and the resistance of the tissues ($R_{tissue}$).

## III. Results

### A. Simulations

The $R_{XY}$ parameters of the two-port network model obtained using the FEM simulation were: $R_{11}$ = 58.8 Ω; $R_{12}$ = 13.9 Ω; and $R_{22}$ = 322 Ω ($R_{tissue}$). These values were replaced in the SPICE schematic shown in Fig. 3, to simulate the behavior of the implant circuitry, and the external system. The burst generator was set at a frequency of 3 MHz, amplitude of 25 V and a burst duration of 100 µs.

Fig. 6 shows the voltage across the implant electrodes for the SPICE simulation. When measured from the LPF of the external system, the attenuation between the measurement made from the DAQ ($v_L(t)$ in Fig. 3) and the voltage measured across the implant electrodes (Fig. 6) was approximately 31 dB.

As the temperature was increased from 35 °C to 40 °C, the time constant $\tau'$ measured at $v_L(t)$ decreased (see Table I). The resistance of $NTC_{im}$ could be calculated as

$$\mathrm{NTC_{im}}' = \frac{\tau'}{\mathrm{C_{im}}} - \mathrm{R_{tissue}} \tag{5}$$

and the temperature could be calculated as

$$T = \frac{1}{\ln\frac{\mathrm{NTC_{im}}'}{R_0}/\beta + \frac{1}{T_0}} \tag{6}$$

Table I shows the results of the temperature measurement after calibrating to cancel the zero-drift. The maximum relative error obtained was 0.25%.

TABLE I. Temperature Measurement in SPICE Simulations

| Defined temperature | Results obtained with two-port network | | |
|---|---|---|---|
| | *Time constant (µs)* | *$NTC_{im}$' (Ω)* | *Temperature (°C)* |
| 40 °C | 13.06 | 984.00 | 40.04 |
| 39 °C | 13.50 | 1027.90 | 39.09 |
| 38 °C | 14.07 | 1085.00 | 37.93 |
| 37 °C | 14.54 | 1131.60 | 37.03 |
| 36 °C | 15.12 | 1190.20 | 35.96 |
| 35 °C | 15.71 | 1248.60 | 34.95 |

### B. In vitro validation

The bursts generator was configured to deliver sinusoidal HF bursts with a frequency of 3 MHz, burst amplitude of 25 V, burst duration ($B$) of 100 µs, and burst period of 1 ms ($F$ = 1 kHz). This corresponds to a peak electric field of 250 V/m (56 $V_{rms}$/m), lower than the maximum allowed

induced *in situ* electric field. According to (4), the applied SAR was 1.68 W/kg, lower than the lowest limit established by the safety standards (i.e., 2 W/kg).

Fig. 7 shows the average of 100 acquisitions obtained by the DAQ ($v_L(t)$) for a reference temperature of 37.7 °C, and the exponential fit obtained of this averaged signal. The time constant $\tau'$ was obtained using the resulting coefficients of the exponential fit. $R_{tissue}$ may vary in the *in vitro* setup due to the electrical conductivity dependence on temperature variations [16]. For this reason, the value of $R_{tissue}$ was neglected in (5), and the temperature was calculated using (6). For this particular case, the temperature obtained with the injectable sensor after zero-drift calibration was 37.5 °C.

Table II shows the calculated time constant $\tau'$, the equivalent resistance for $NTC_{im}'$, and its corresponding temperature after calibrating to cancel the zero-drift. The maximum relative error obtained was 2.02%. Fig. 8 shows the exponential fit obtained for some temperature measurements reported in Table II.

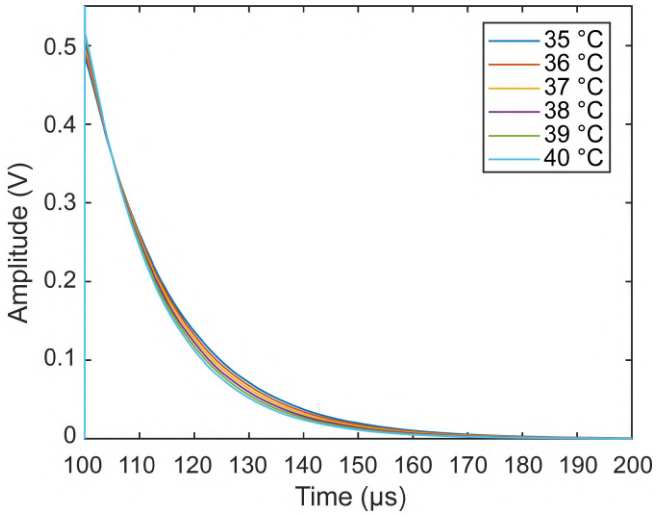


Fig. 6. SPICE simulation of the voltage across the implant electrodes using the two-port network shown in Fig. 3, just after the burst cessation.

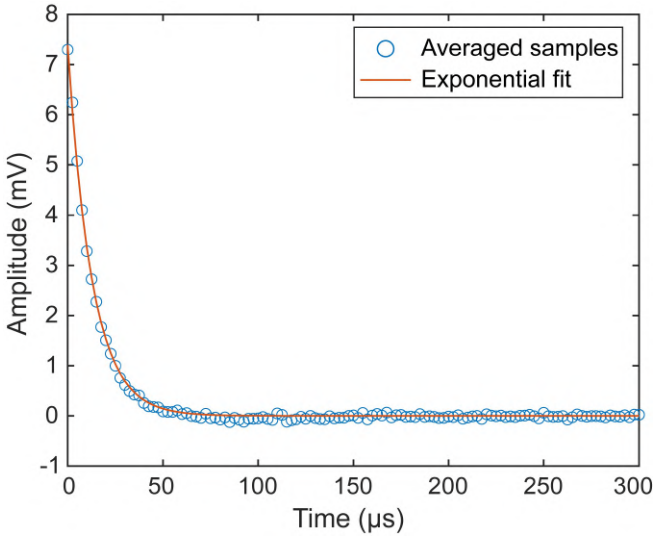


Fig. 7. Example of averaged discharge from 100 bursts cessations obtained by the external unit using the *in vitro* setup shown in Fig. 5 and the injectable prototype. The temperature measured with the reference thermistor was 37.5 °C; while the injectable device measured 37.7 °C.

TABLE II. TEMPERATURE MEASUREMENT IN *IN VITRO* SETUP

| Reference temperature | Results obtained with implant | | |
|---|---|---|---|
| | *Time constant (µs)* | *Resistance (Ω)* | *Temperature (°C)* |
| 40.2 °C | 11.583 | 1158.33 | 39.4 |
| 38.7 °C | 11.917 | 1191.67 | 38.8 |
| 38.3 °C | 12.167 | 1216.67 | 38.4 |
| 37.7 °C | 12.667 | 1266.67 | 37.5 |
| 34.2 °C | 14.833 | 1483.33 | 34.3 |
| 33.8 °C | 15.083 | 1508.33 | 33.9 |

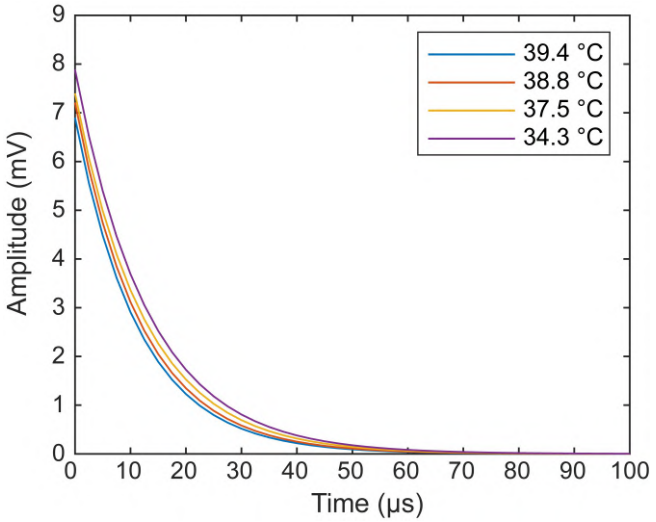


Fig. 8. Example of exponential fit obtained by the external unit for different temperatures after averaging 100 sequential acquisitions using the *in vitro* setup and the injectable sensor (Fig. 4). The temperatures displayed are the result of zero-drift calibration.

## IV. DISCUSSION AND CONCLUSIONS

The geometry used in the simulations and *in vitro* assays shows that it is possible to obtain measurements with implant depths of 3.25 cm. According to preliminary simulations not reported here, the implantable sensor could give measurements with depths higher than 5 cm using the highly specific geometry shown in Fig. 5. However, this scenario does not include the dielectric properties of different types of tissues. Further analysis must be done in this sense, as that reported in [17].

The maximum relative error obtained in simulations is low enough for accurate continuous temperature monitoring in biomedical applications. However, for the *in vitro* calculation of the equivalent resistance of $NTC_{im}'$ in (5), the tissue resistance ($R_{tissue}$) was neglected as the electrical conductivity of the medium changes with temperature. One way to avoid the dependence on the conductivity is to replace the $NTC_{im}$ used, with a thermistor that has higher $R_0$. In this way, the value of $NTC_{im}$ is much higher than that of $R_{tissue}$ in (5). However, this would decrease the decaying voltage seen from the external electrodes ($v_L(t)$), hindering the measurement of the time constant, and the corresponding temperature. Another way to avoid this dependency on $R_{tissue}$ is to add to the implant a current controlled discharge

network, as a JFET current limiter ($JFET_{im}$ in Fig. 9). This makes the discharge independent of the impedance of the electrodes and the tissue in a limited time frame.

In the case of the external unit that interrogates the implants, the amplitudes obtained for $v_L(t)$ immediately after burst cessation are in the order of the mV, and may have a low signal-to-noise ratio (SNR). This is overcome with the proposed signal processing consisting in averaging multiple burst cessations ($v_L(t)$), and doing an exponential fit to find the time constant and the equivalent resistance.

The proposed method is an alternative to other passive interrogation approaches, and to active interrogation methods supported by WPT strategies not based on volume conduction. Ultrasonic WPT has been emerging as a strategy to power or interrogate implants, such as the temperature sensor reported in [5]. However, this method presents 1) lower implantation depths (e.g., only 2 cm in [5]) because of its intrinsic focal characteristic, 2) the need to use gel which may cause irritation in chronic applications, and 3) the unknown effects related to the long-term exposure to ultrasounds. This limits its use in sensing applications, and as WPT alternative for active implantable medical devices.

The novel, ultrathin and flexible temperature sensor prototype demonstrated here consists in a very thin and flexible passive device that could be easily implanted by injection using a 14 G catheter, as shown in [10]. Its geometrical properties make it suitable for implantation in different body tissues, allowing its use in limited spaces, while avoiding disrupting the physiological functions happening in the surroundings. The sensor could be the basis for a safe and accurate device that does continuous and *in situ* temperature monitoring. This opens the possibility of using the technology for different biomedical applications in which temperature sensing directly on the target location could improve and accelerate diagnosis and treatment, improving the quality of life of patients.

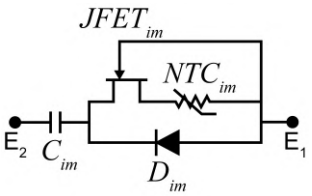


Fig. 9. Passive temperature sensor proposed for avoiding dependency of tissue resistance. The sensor includes a current controlled discharge network.

## ACKNOWLEDGMENT

This project has received funding from the European Research Council (ERC) under the European Union's Horizon 2020 research and innovation programme (grant agreements No 724244 (eAXON) and 963955 (SENSO-eAXON)), and the UPF INNOValora programme, which is co-financed by the Generalitat de Catalunya and the European Regional Development Fund. Antoni Ivorra gratefully acknowledges the financial support by ICREA under the ICREA Academia programme.

## REFERENCES

[1] G.-Z. Yang, Implantable sensors and systems: From theory to practice, 1st ed. Springer International Publishing, 2018.

[2] A. Chanmugam et al., "Relative Temperature Maximum in Wound Infection and Inflammation as Compared with a Control Subject Using Long-Wave Infrared Thermography," Adv. Skin Wound Care, vol. 30, no. 9, 2017.

[3] W. Hasenkamp et al., "Design and test of a MEMS strain-sensing device for monitoring artificial knee implants," Biomed. Microdevices, vol. 15, no. 5, pp. 831–839, 2013.

[4] F. Graichen, G. Bergmann, and A. Rohlmann, "Hip endoprosthesis for in vivo measurement of joint force and temperature," J. Biomech., vol. 32, no. 10, pp. 1113–1117, 1999.

[5] C. Shi et al., "Application of a sub–0.1–mm implantable mote for in vivo real-time wireless temperature sensing," Sci. Adv., vol. 7, no. 19, p. eabf6312, May 2021.

[6] L. Perl et al., "A Novel Wireless Left Atrial Pressure Monitoring System for Patients with Heart Failure, First Ex-Vivo and Animal Experience," J. Cardiovasc. Transl. Res., vol. 12, no. 4, pp. 290–298, 2019.

[7] M. J. Weber, Y. Yoshihara, A. Sawaby, J. Charthad, T. C. Chang, and A. Arbabian, "A Miniaturized Single-Transducer Implantable Pressure Sensor With Time-Multiplexed Ultrasonic Data and Power Links," IEEE J. Solid-State Circuits, vol. 53, no. 4, pp. 1089–1101, Apr. 2018.

[8] Y. Kifle, J. Wikner, J. Zötterman, L. Rydén, and S. Farnebo, "NFC Powered Implantable Temperature Sensor," in 2019 41st Annual International Conference of the IEEE Engineering in Medicine and Biology Society (EMBC), 2019, pp. 4359–4362.

[9] Abbott Cardiovascular, "PROCEDURE OVERVIEW Implanting the CardioMEMS PA Sensor," 2021. [Online]. Available: https://www.cardiovascular.abbott/us/en/hcp/products/heart-failure/pulmonary-pressure-monitors/cardiomems/procedure-overview.html.

[10] S. Malik et al., "Injectable Sensors Based on Passive Rectification of Volume-Conducted Currents," IEEE Trans. Biomed. Circuits Syst., vol. Early acce, 2020.

[11] "IEEE Standard for Safety Levels with Respect to Human Exposure to Electric, Magnetic, and Electromagnetic Fields, 0 Hz to 300 GHz." IEEE, 2019.

[12] C. Gabriel and S. Gabriel, "Compilation of the Dielectric Properties of Body Tissues at RF and Microwave Frequencies.," 1996.

[13] S. R. Ward and R. L. Lieber, "Density and hydration of fresh and fixed human skeletal muscle," J. Biomech., vol. 38, no. 11, pp. 2317–2320, 2005.

[14] L. Becerra-Fajardo, M. Tudela-Pi, and A. Ivorra, "Two-Port Networks to Model Galvanic Coupling for Intrabody Communications and Power Transfer to Implants," in 2018 IEEE Biomedical Circuits and Systems Conference (BioCAS), 2018, pp. 1–4.

[15] A. C. Paglinawan, Y.-H. Wang, S.-C. Cheng, C.-C. Chuang, and W.-Y. Chung, "CMOS temperature sensor with constant power consumption multi-level comparator for implantable bio-medical devices," Electron. Lett., vol. 45, no. 25, pp. 1291–1292, 2009.

[16] J. A. Sorensen and G. E. Glass, "Ion and temperature dependence of electrical conductance for natural waters," Anal. Chem., vol. 59, no. 13, pp. 1594–1597, 1987.

[17] M. Tudela-Pi, J. Minguillon, L. Becerra-Fajardo, and A. Ivorra, "Volume Conduction for Powering Deeply Implanted Networks of Wireless Injectable Medical Devices: A Numerical Parametric Analysis," IEEE Access, vol. 9, pp. 100594–100605, 2021.